

ARTICLE

Bringing depth to scanning tunnelling microscopy: subsurface vision of buried nano-objects in metals

Received 01th March 2022,
Accepted 00th Month 20xx

DOI: 10.1039/x0xx00000x

Oleg Kurnosikov*^{a, b}, Emilie Gaudry^a, Muriel Sicot^a, Danielle Pierre^a, Yuan Lu^a, Stéphane Mangin^a

Abstract

A method for subsurface visualization and characterization of hidden subsurface nano-structures based on Scanning Tunneling Microscopy/Spectroscopy (STM/STS) has been developed. The nano-objects buried under a metal surface up to several tens of nanometers can be visualized through the metal surface and characterized with STM without destroying the sample. This non-destructive method exploits quantum well (QW) states formed by partial electron confinement between the surface and buried nano-objects. The specificity of STM allows for nano-objects to be singled out and easily accessed. Then, their shape, size and burial depth can be determined by analysing the spatial distribution and oscillatory behavior of the electron density at the surface of the sample. The proof of concept was demonstrated by fabricating argon nanoclusters embedded into a single-crystalline Cu matrix. Taking advantage of the specific electronic band structure Cu and inner electron focusing, we experimentally demonstrated that noble-gas nanoclusters of several nanometers large buried as deep as 80 nm can be detected, characterized and imaged. The ultimate depth of this ability is estimated as 110 nm. This approach using QW states paves the way for an enhanced 3D characterization of nanostructures hidden well below a metallic surface.

New concept

It is of common belief that STM/STS is a characterization method applied exclusively to a surface or objects on it. However, some reports show that subsurface single atomic impurities or shallow nanostructures could be recognized with STM as well. The presence of such objects in close proximity to the surface would induce a tiny surface deformation or a perturbation of the local density of electronic states (LDOS) at the surface, which can actually be detected with STM/STS. The embedded objects, detected by a local change in surface properties, are reported to be no more than a couple of nanometres below the surface. So far, the question of how deep an STM can in principle detect the hidden objects below a surface has never been considered. The actual study demonstrates the depth record of about one hundred of nanometers achieved at visualization of subsurface nanoclusters in a metallic sample with STM. To get this extremely deep STM-vision, we exploit QW states formed by delocalized electron states confined between the surface of the metal and the local interface with the nanoclusters. Additionally, we profit from electron focusing of bulk electronic states due to an appropriate band structure of the metal. The spatial variation and the oscillations of conductance spectra measured by STS at the surface allows to determine the location, depth, and size of the buried nanoclusters, as well as to indicate their shape. Our approach paves the way for non-destructive STM characterization of buried nanostructures and triggers the development of 3D subsurface nano-analysis with STM.

Introduction

Scanning tunnelling microscopy (STM) and spectroscopy (STS) have become a widely used technique for imaging surface structures with atomic resolution [1] and determining the local

density of electronic states (LDOS) of surface atoms, molecules or nanostructures [2]. The extremely high surface sensitivity of this technique is a direct consequence of a strong exponential decay of the probability of tunnelling selecting the atoms closest to the tip. Therefore, it is commonly believed that an STM can be used exclusively for characterization of a surface as well as atomic, molecular and nanostructures on it. For profiling structures below a surface, the STM still can be used together with sample-destructive post-processing like milling [3] or cleaving the sample [4]. This destructive post-processing forms a new surface from deeper layers of materials or in cross-

^a Université de Lorraine, Institut Jean Lamour, France.

^b ex. Technische Universiteit Eindhoven, department of Applied Physics, Netherlands.

* Contact address: Oleg.Kurnosikov@univ-lorraine.fr

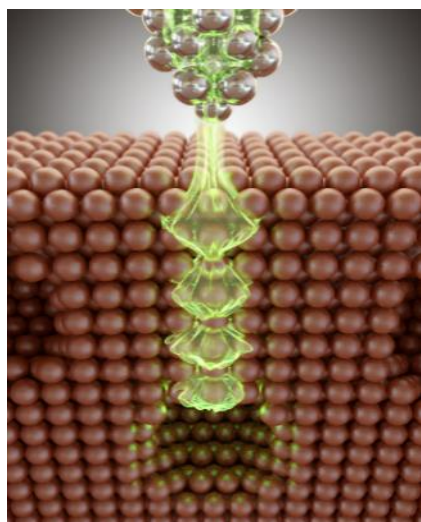


Fig. 1 Illustration of the concept of subsurface STM vision based on the near-surface resonances of non-localized electronic states of the matrix material.

sections and then STM performs the surface characterization on them. This way for accessing deeper structures is widely used also for depth profiling study with transmission electron microscopy [5], scanning electron microscopy [6], as well with electron spectroscopy [7]. However, this sample-destructive technique has drawbacks as the interfaces an embedded structures can be damaged during the sample post-processing. Frequently, the destructive post-processing has to be performed in several stages or with a set of the samples for detailed characterization.

In this article, we develop the subsurface STM/STS vision through a metallic surface for characterisation of the nano-objects buried up to 100 nm below the surface excluding any sample-destructive post-processing like milling or cleaving. Our approach allows to see the nano-objects at different depths with one STM scan and to determine their location, depth size and even shape. Avoiding any sample-destructive post-processing gives an opportunity to follow the evolution of the systems with embedded nano-objects in time under different activation processes.

The ability of the STM to indicate in its images the presence of subsurface objects was demonstrated previously, but it was not widely used for subsurface characterisation. There are some examples of STM images showing that tiny deformations of the surface or an appearance of additional electronic states at the surface can be attributed to subsurface atoms or nanostructures buried [8, 9, 10] one or a couple atomic layers below a surface. In semiconductors, near-surface impurities are recognized as extra features superimposed onto the STM images of a surface [4, 11–14]. Such effects can become very spectacular in the case of single dopants in semiconductors since the embedded charges and states of the dopants are not screened over the distance of several nanometers and therefore contribute directly to the LDOS at the surface [15].

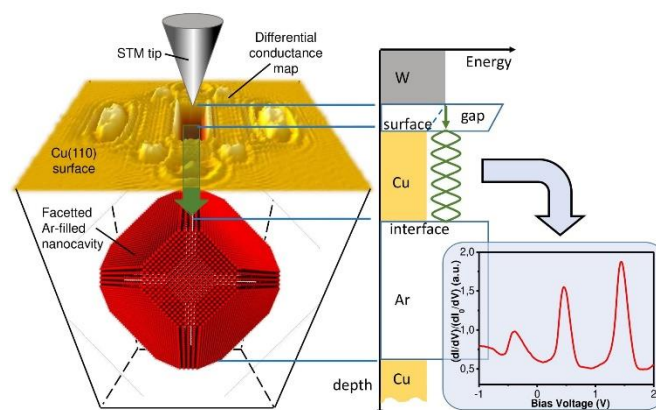


Fig. 2. Schematic drawing of realisation of the subsurface detection of hidden nanocluster. Left panel illustrates the configuration of the system and lateral distribution of the surface conductance induced by the subsurface nanocluster with a faceted interface. The middle panel is the corresponding energy diagram leading to the measured oscillatory behaviour of the normalized differential conductance in STS spectrum displayed in the bottom right panel.

As a contrary, in materials with a very high electron density like metals, such subsurface impurities and defects buried several nanometers underneath can not be detected as easily since their states and charges are screened already over the interatomic distances. As a consequence, subsurface STM vision at the depth on the nanometre scale in metals is considered to be unrealistic.

In this article, we oppose this statement by presenting an experimental evidence of the extremely deep subsurface vision in metals with STM. Instead of direct detection of the localized electronic states belonging to the buried impurities or nanostructures we use bulk non-localized states of the host material (Fig. 1). The electron density of the bulk between the surface and the buried nano-object gets the oscillating component and this component can be probed with STS at the surface near the location of the hidden nanoobject. Because the length of delocalization of these states can be very large, a deep subsurface structure can be detected.

Previously, several STM experiments reported the use of LDOS oscillations in a metallic layer for the subsurface detection and thus confirm the validity of this approach. For example, the steps at Si substrate covered with a flat Pb layer were imaged by analysing LDOS variation on the flat surface of lead [16–23] whereas the same effect was also observed with thin films of Cd [24]. A similar concept has been used by Weissman *et al.* [25] and Kotzot *et al.* [26]. They were able to locate subsurface impurity atoms buried several atomic layers below the Cu surface by treating the diameter of oscillating LDOS rings. The spatial oscillations of LDOS induced by electron scattering at a subsurface atom is theoretically described by Avotina *et al.* [27] and Lunis *et al.* [28]. There are also a few examples of imaging the subsurface nanoobjects showing stronger signal due to

efficient reflection. The systems are represented by nanocavities formed in metals like Cu, Pb, Ag or Al and filled in by noble gases [29-36]. However, the typical depth of location of subsurface structures in these reports does not exceed a couple of nanometers while the signals still reveal remarkable and measurable oscillations in LDOS. This indicates that the limit in the depth has not been achieved.

In this article, we show that the limit of subsurface vision can be pushed in one or two orders more than previously reported. For illustration, we exploited an ideal system which was used in pioneering works of Adam *et al.* and Kurnosikov *et al.* [33-35], however they reported only some particular results. Our approach of the subsurface STM vision provides not only the detection of subsurface structures at a given location but determines also their depth and size with a precision better than 1 nm and getting some indication of their shape. Understanding of all limiting factors allowed us to achieve the depth of subsurface vision in our experiments up to to 80 nm and estimate the ultimate depth of detection of around 110 nm.

Principles

As well known, the LDOS could be accessed by means of STS at the surface [2]. The LDOS at the surface is usually determined by the band structure of material at corresponding crystallographic orientation, by the states associated with the crystal termination, so-called surface states, and by localized states of single atoms or molecules in- and on the surface. The last type of states is mostly used for the visualization of atomic structure in STM images, whereas the two first ones usually contribute to a homogeneous background, which meets much less of interest in STM applications. However, in some cases the delocalized states can reveal interesting features in the STM/STS images. Regarding a system with *surface delocalized* states, for example the stepped surface of Cu(111) or the same surface with surface impurities, standing wave patterns of electron density can be observed on STS maps [37]. The standing waves surround the impurity atoms or group near the step edges since they originate from the scattering of delocalized electrons on these objects and electron wave interference. Exactly the same mechanism of formation of standing wave of electron density should be realized also in volume for *bulk delocalized* electronic states in case of the scattering or reflection from the objects located in the bulk, *i.e.* below the surface. In this case, however, the deep subsurface object cannot be reached with the STM probe and therefore does not appear in STM images. Nevertheless, the perturbation of the spectra of delocalized bulk states due to subsurface scattering can be observed *at the surface* as well. The perturbation of the spectra appears as superimposed electron density oscillations across the surface as well as the oscillation of electron density probed in a selected location versus energy since the electrons at the scattering obey a wave equation. Considering the scattering from a bigger subsurface object, like an interface with some buried nanocluster and a free flat surface, one can expect a multiple electron reflections between them. In this case, the interface and surface serve as boundaries partially confining the delocalised bulk electrons. The partial

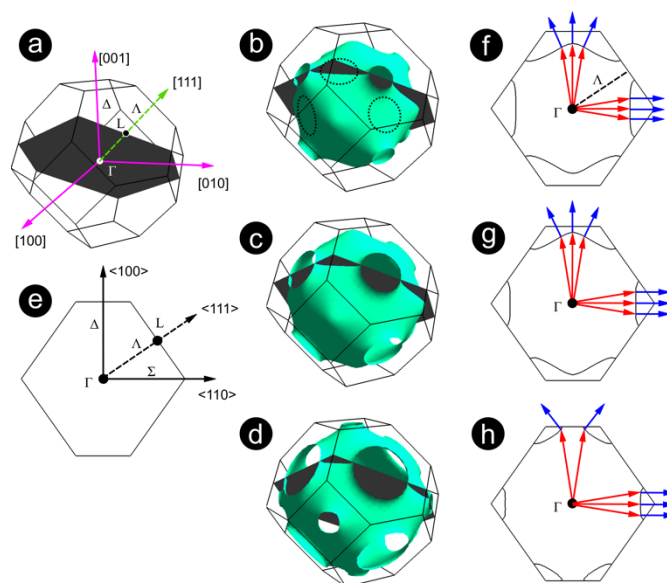


Fig.3 Principles of electron focusing in Cu: (a) First Brillouin zone (BZ) of an *fcc* lattice with relevant high-symmetry *k*-points, directions and lattice vectors. The grey plane is $[1/2, 1/2, 1]$; (b-d) Iso-energetic surfaces obtained from the calculated band structure of Cu in reciprocal space at (b) Fermi level, E_F (Fermi surface), (c) $E_F + 1$ eV and (d) $E_F + 2$ eV. The encircled areas in (b) highlight the saddle zones close to the $\langle 110 \rangle$ directions that are locally almost flat. (e) Cross-section between the grey plane and the first BZ in (a); (f-h) Cross-sections related to the grey plane $[1/2, 1/2, 1]$ in (a, e) at the corresponding energies (f) E_F , (g) $E_F + 1$ eV, and (h) $E_F + 2$ eV, respectively. Red arrows illustrate *k*-vectors in the $\langle 110 \rangle$, $\langle 100 \rangle$, and close to them directions. Blue arrows indicate the directions of the group velocity. The propagation of electron waves with *k*-vectors around the $\langle 110 \rangle$ are almost parallel, whereas it diverges for electron packages with *k*-vectors close to the $\langle 100 \rangle$.

confinement could lead to a formation of localized near-surface quantum well (QW) resulting in much stronger quasi-periodical variation of the electron density. A schematic representation of such a geometry and its corresponding energy landscape is given in Fig.2. Therefore, the observation of *oscillatory component* in LDOS revealed by STS above the buried nanostructure can be used for the detection of buried nanoparticle. Moreover, by analysing the period of oscillation ΔV , it would also be possible to determine depth d of confinement of the bulk states that is also the depth of the corresponding facet of the subsurface structure, using the following formula:

$$d = \pi (dE/dk) \cdot 1/(e\Delta V) \quad (1)$$

where dE/dk is derivative of energy E by the wave vector of electrons k in the appropriate direction deduced from the band structure and e is the electron charge. Beside the depth of location, also the shape or size of the subsurface structure can be reconstructed considering the lateral variation of LDOS with a corresponding model [33-34].

Thus, the ability to detect and characterize the subsurface nanoclusters is based on the presence of the oscillatory component of LDOS in STS signal. The amplitude of this component and its oscillation period decrease with d increase. Therefore, an ultimate depth of detection would be defined as the depth when the oscillations are no longer recognizable in STS measurements.

Several factors are responsible for the formation of oscillations and thus determining the ultimate depth of STM vision, namely the electronic coherence length, interface roughness, and the electronic band structure of the host material, as discussed below.

First, since the subsurface vision is based on the electron interference, the oscillation whose period is used to determine the depth d as expressed in formula (1) can occur if the depth does not exceeds the coherence length of the corresponding states. This coherence length is known to vary with the electronic mean free path (MFP). This last parameter, which is material-dependent, is limited by electron scattering on phonons, impurities or due to other collective interactions. Therefore, it varies with temperature T , impurities concentration, and electron energy. Overall, the MFP ranges from a few nanometers to several tenth of nanometers [38, 39]. Temperature modifies MFP such that MFP gets even much longer with T decrease. It is also noteworthy that temperature affects the broadening of the LDOS oscillation peaks belonging to each QW resonances. As a consequence, T will have an influence on the ultimate depth detection.

Second, the coherence can also be partially or completely lost at the reflection due to a rough interface. Therefore, buried nanostructures forming atomically flat interfaces with the host material are more likely to be detected with STM.

Third, the electronic band structure of the host material is important as well in determining the ultimate depth of detection. Its angular distribution is responsible for the divergence and decay of the electronic state packages since an STM probes the states with some variety of k -vectors in the three-dimensional reciprocal space. The decay depends on the direction of electron wave packages propagation in the bulk. As well known, the direction of propagation of wave package in the bulk at low energy is determined by the vector of group velocity $\mathbf{v}_g(\mathbf{k})$:

$$\mathbf{v}_g(\mathbf{k}) = \nabla_{\mathbf{k}} E(\mathbf{k}) \quad (2)$$

where the electronic dispersion relations $E(\mathbf{k})$ can be determined theoretically or experimentally in the form of electronic band structures [40]. According to formula (2), at a specific energy E_0 that can be experimentally set with STM choosing a bias voltage V_0 such that $E_0 = eV_0$, in reciprocal space, the group velocity \mathbf{v}_g is perpendicular to the iso-energetic surface of the host material. In case the bias is set to zero, the energy dispersion surface corresponds to the Fermi surface. In previous works [27, 28, 41, 42], it has been shown that the contours of the Fermi surface affect the direction of the group velocity. Specifically, when injecting electrons into directions where the Fermi surface is almost flat, the group velocity stays

parallel for some close range of \mathbf{k} . This effect has been called the focusing effect. On the contrary, where the Fermi surface has a more spherical shape, the group velocity tends to diverge and as a consequence, the propagation directions are more spread. This has been illustrated experimentally in the case of single Co atoms embedded into a Cu(111) single crystal and theoretically explained using the Fermi surface of Cu [25, 28]. However, as the period of LDOS oscillations versus bias voltage is needed to determine the depth at which the object is buried, it is of paramount importance to not only consider the Fermi surface but contours at all energies within the range of the measure typically corresponding up to 2eV for a regular STS spectrum. Therefore, we have calculated iso-energy surfaces for Cu in the First Brillouin Zone shown in Fig.3(a) setting the energy to the Fermi level E_F , $E_F + 1\text{eV}$, $E_F + 2\text{eV}$ as displayed in Fig. 3(b-d), respectively. In good agreement, with previous studies [25, 27, 28], the Fermi surface of Cu bear very flat regions with strongly suppressed curvature in $\langle 110 \rangle$ directions whereas necks resulting from band gap opening are observed in $\langle 111 \rangle$ directions around L points. In addition, energy bumps can be found in $\langle 100 \rangle$ directions around X points. Those three features remain valid within the range of 0-2eV as displayed in Fig. 3(b-d), respectively though the flat areas around Σ shrink with increasing energy due to the larger opening of the band gaps at L points. In order to better understand the influence of such contours on the focusing effect, we now discuss the anisotropy of the propagation of electronic waves in the STM experiment by looking at the group velocity as a function of the energy. To do so, we have chosen to consider a cross section between the plane $[\frac{1}{2} \frac{1}{2} 1]$ which contains the main 3 high-symmetry directions (see grey plane in Fig. 3(a) and its planar presentation in Fig. 3(e)) and the constant energy surfaces of Fig.3(b-d). The resulting cross-sections are displayed in Fig. 3(f-h) where red arrows illustrate \mathbf{k} -vectors whereas blue arrows indicate the group velocity giving the indication of the propagation direction, which is perpendicular to the contour displayed as black solid line. Obviously, upon increasing energy (*i.e.* bias voltage in STM experiment), the group velocity \mathbf{v}_g remains parallel to the $\langle 110 \rangle$ direction for the \mathbf{k} -vectors grouping around $\langle 110 \rangle$. However, if the corresponding \mathbf{k} -vectors lie around the $\langle 100 \rangle$ direction, the divergence of \mathbf{v}_g occurs due to the presence of an energy bump in the reciprocal space. This translates into the fact that if electrons are injected into a (110)-cut surface, they will propagate mostly following that direction keeping the same amplitude over a long distance. However, their injection into the (001)-cut surface will result in a stronger decay due to the spatial divergence of corresponding propagating states. This discussion could be generalized to any other materials: flatness of the contour of iso-energetic surface would lead to a focusing effect of the injected electrons [41, 42].

Since the local flatness of the iso-energetic surface of copper in $\langle 110 \rangle$ allows to concentrate the electronic states in this direction, the oscillating STS signal should be more pronounced and it would be worth to use this direction for enhancing the ultimate depth of the subsurface electron vision.

Experiment

Considering the abovementioned conditions, to illustrate the principles of the subsurface vision at ultimate depth, we chose the system composed of a high purity Cu single-crystal as the host material which cut is in the (110) direction and provides a maximum focusing effect. Copper is a material with well-determined characteristics such as band structure and electronic MFP. The buried nano-objects are argon nanoclusters. As they are not conductive, they provide the full reflection at the interface with copper. Since the atomic electronic structure of Ar does not play any remarkable role in the electronic processes we consider, we can reasonably treat the Ar nanoclusters in Cu also as nanocavities with Ar filling.

The Ar nanoclusters in copper are formed by irradiating the (110) surface of Cu single crystal with a dose of $2 \cdot 10^{17} \text{ cm}^{-2}$ of Ar^+ ions with a kinetic energy of 5 keV. This ion energy was specifically chosen since it leads to a penetration of Ar into Cu up to 10 nm. In order to recover an atomically flat surface of Cu after irradiation with Ar, a moderate annealing at 1050K for 5 min was performed. During this post-annealing, Ar segregation occurs. As a consequence, a significant part of the implanted Ar atoms reaches the surface and leaves the sample. However, some amount of the embedded Ar remains in copper forming nanoclusters of a typical size of around 2 - 5 nm. As we needed Ar nanoclusters buried deeper than those obtained after the thermal treatment, we deposited extra layers of Cu with increments of 10 nm thickness. A slight annealing to recover a flat Cu surface followed each post-deposition. The deposition was done with a calibrated effusion cell EFM3. Between each step, the sample was scanned with STM to visualise the nanoclusters. Since the van der Waals binding of Ar atoms in the clusters is much weaker than the binding of Cu atoms in the metallic crystalline lattice, the shape of the subsurface nanoclusters is determined to a great extent by the anisotropy of the surface tension of the Cu crystal. This provides Wulff

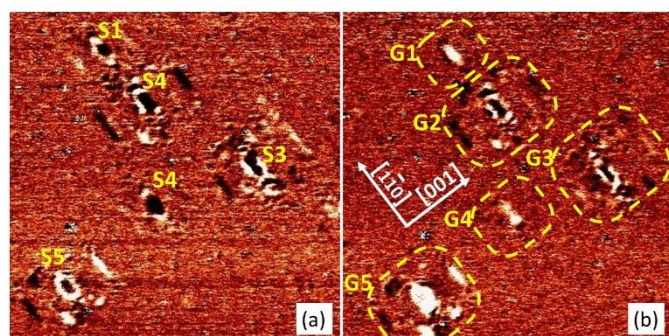


Fig.4 Differential conductance distribution across the Cu surface (STS map), $45 \times 45 \text{ nm}^2$, at two different bias voltages: (a) 100 mV and (b) 150 mV and the tunnel current of 1.5 nA. The spots in the same positions change their contrast with bias voltage. The spots can be grouped in the uniformed ensembles of a main spot and a few satellite spots, as countered with the dashed lines. Satellite spots around some weak main spots somewhere are not well resolved.

construction [43] of the nanoclusters in the inversed form: a hollow polyhedron with the determined facets shape. Figure 2 presents the expected shape of the last atomic layer of copper at the interface with the Ar nanocluster deduced from an estimation of the anisotropy of the Cu surface energy as well as from some experimental data [44, 45]. The atomically flat facets at the interface serve as ideal reflectors for the delocalised electron states outside the nanocluster. One of the rectangular {110} facets is parallel to the surface. On one hand, the (110) facet is the smallest one and would provide less efficient electron confinement in between the interface and surface, but on the other hand, the $\langle 110 \rangle$ direction leads to the most efficient focusing of electron states as mentioned previously and should favour the most intense oscillating reflected signal. The STM/STS measurements were done using a low-temperature STM microscope "Omicron" at temperatures of 77K and 4.7K under ultra-high vacuum. To get reliable STS measurements, we carefully conditioned the STM tips by means of local e-beam annealing. This process was controlled by checking the cold field emission from the tip. With this procedure, we were able to obtain repeatable and reliable oscillatory behaviour of the LDOS. Nevertheless, we cannot exclude some dispersion among STS spectra that could originate from the variety of the tip states at the very apex of different STM probes.

Results and discussion

After preparation, large scale STM images of the Cu(110) surface exhibit large atomically flat terraces separated by single atomic steps. With such a surface, one would reasonably expect a homogenous distribution of LDOS across the terraces, as usually always observed without any argon implantation. Surprisingly, the STS maps at smaller scale reveal a deviation of LDOS from its regular value in many locations on each terrace. Figure 4 shows two STS maps of the same area scanned at two different biases: 100 mV (Fig. 4(a)) and 150 mV (Fig. 4(b)). The locations with deviating LDOS can be described as a system of

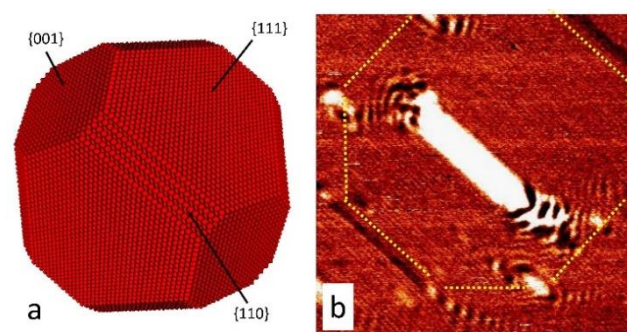


Fig.5 (a) Expected shape of the last layer of Cu interface around Ar nanocluster; (b) High resolution STS map ($16 \times 16 \text{ nm}^2$) above an Ar nanocluster revealing the main oblong spot originated from the {110} facet, and the satellite spots corresponding to the conjunction of the {110}, {111}, and {001} facets, and the conjunction of the {111} and {001} facets. The yellow contour indicates the projected subsurface nanocluster.

spots of various sizes and shapes with different and variable contrasts. Some of the spots, the largest ones, are indexed with letters S1-S5 in figure 4 (a). Depending on the value of bias voltage, the spots in the same locations can be visualized on the STS maps with a lower contrast, for example the spots S1 and S5 at 100 mV (Fig. 4 (a)) or a higher contrast (see the corresponding spots at 150 mV (Fig. 4 (b))). All the spots of different shape and size are uniformly oriented and form reproducible groups encircled with dashed labelled with G1 to G5 in Fig. 4b. The groups are composed of a main oblong spot of the strongest contrast in the centre of the each group flanked by two elongated lines and surrounded by 4 more rounded small satellites spots (Fig. 4 and 5(b)). Remarkably, the oblong main spots as well as line-shaped satellite spots are all well oriented along [1-10] direction. If the main spots appear with a quite low contrast, for example the spots S1 and S4, the satellite spots may be vague at some bias voltages (Fig. 4 (a)) or absent at other bias voltages (Fig. 4 (b)). The spots with oblong shape can exhibit complex differential conductance contrast. As an example, the oblong spot S5 is imaged with a white rim surrounding the dark centre (Fig. 4(a)) corresponding to enhanced and suppressed electron density, respectively. The

oblong shapes of S2 and S3 show more complex features: besides a dark core and white borders, they exhibit in addition an oscillatory contrast in the [1-10] direction also clearly seen for another object in Fig. 5b. The observed spatial oscillation of the contrast and its altering with bias voltage leads to the suggestions that these spots on the STS maps may appear due to near-surface electron scattering. It would be natural to associate each group of the ordered spots with a corresponding Ar nanocluster hidden beneath the surface [35, 36]. The top view from the (110) surface of the idealized Ar nanocluster presented with the first interface Cu layer is depicted in figure 5(a). We demonstrated previously in our work [35] the correspondence between the observed spots and specific facets: the oblong main spot has been shown to be attributed to the parallel upper (110) facet that could reflect the injected electrons back. The satellite spots are induced by the ordered atomic structure in between the {110} and {001} facets whereas the satellite lines are associated with scattering at the edges of {111} facets [35]. In other words, each observed feature can be associated with QW resonances coming from specific facets of the nanocluster. The contour line connecting the small satellite spots and passing through satellite lines gives the exact size and

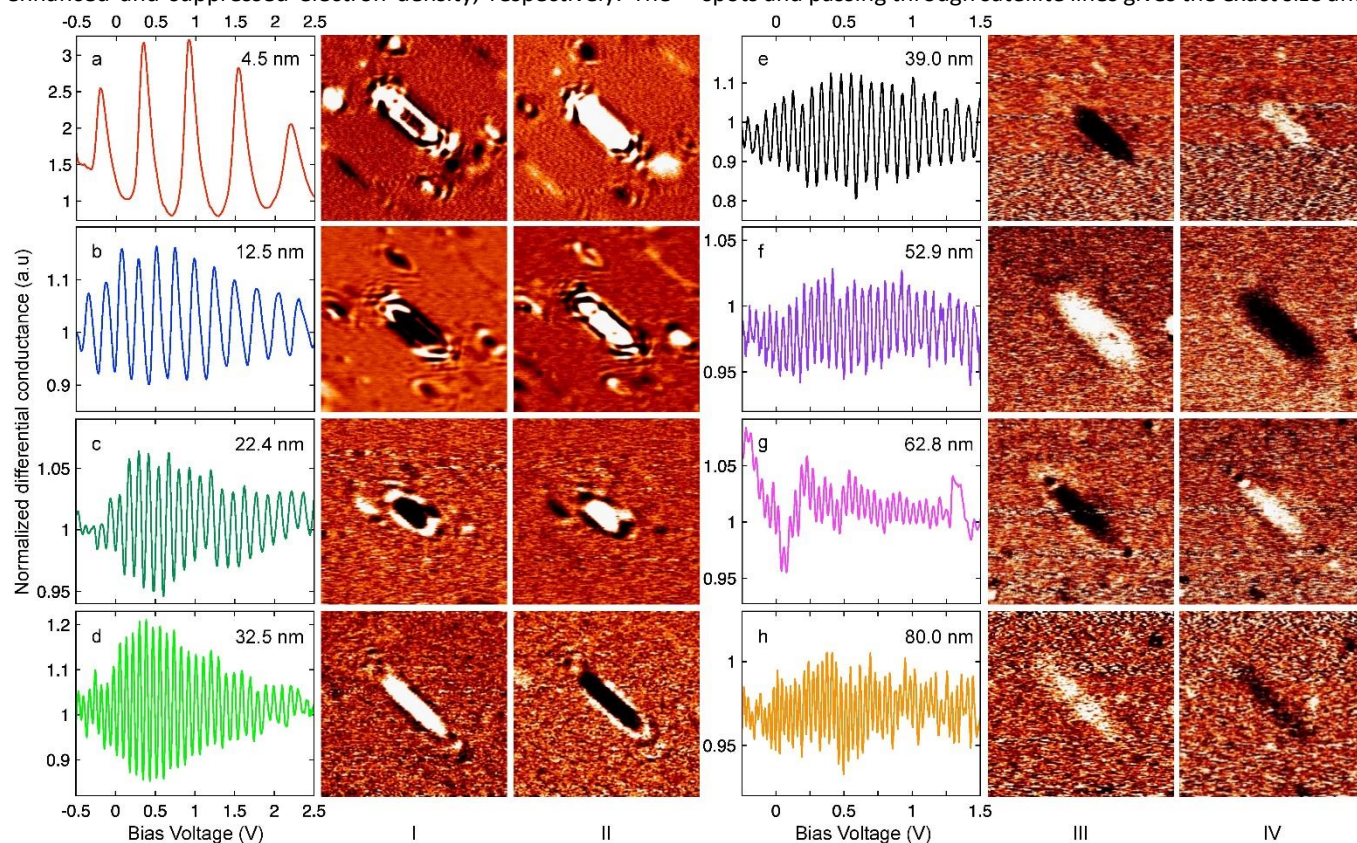


Fig. 6. Evolution of spatially resolved and normalized differential conductance as a function of burial depth: a) 4.5 nm, b) 12.5 nm, c) 22.4 nm, d) 32.5 nm, e) 39.0 nm, f) 52.9 nm, g) 62.8 nm, and h) 80.0 nm. For each specific depth (a - h), three panels show: oscillating normalized differential conductance versus bias voltage measured in the centre of the main spot, and two maps of differential conductance (columns I, II (a-d) and columns III, IV (e-h)) recorded at two different bias voltages showing the corresponding spot with opposite contrasts. The contrast and oscillation amplitude at the depth of 80 nm (h) are high enough to detect the buried nanocluster. The shape and size of the main spot can be used to judge the size of the deep subsurface nanocluster if the satellite spots are not observed.

shape of the nanocluster (Fig. 5(b)). As explained previously, the actual contour may appear slight asymmetrical due to deviations from the idealized shape of the nanocluster as in Fig. 5(a). However, the simple observation the spots and connecting the features on the STS maps to size and shape of hidden subsurface nanoclusters says very little about the depth of location. To obtain this parameter, we should extract the oscillating component of the LDOS versus bias voltage and apply formula 1.

Since the origin of the spots is established, the measurement of differential conductance only in the centre of main oblong spot associated with the closest (1-10) facet in each group is sufficient to determine the location of Ar nanocluster. The sets of these measurements for different depths is presented in figure 6. The set of measurements is performed with the sample after the deposition of each layer of copper in increments as described above. By this process of fabrication and analysis we aimed at practical demonstration of ultimate depth of STM subsurface vision.

First, the differential conductance measured in the centre of main spot for all the depths (Fig. 6, see plots) clearly reveal remarkable oscillations versus bias voltage with the periodicities specific for each depth. This directly proves our suggestion connecting the observed spots with the subsurface scattering or QW resonances. Additionally, two STS maps with the corresponding buried nanocluster are shown on the right of each plot of oscillating normalized differential conductance in figure 6. The maps were recorded at two voltage biases corresponding to one maximum and one minimum of the differential conductance and therefore the main spots demonstrate the opposite contrasts. This also gives better understanding of the variety of contrasts for different spots observed in Fig. 4: due to the difference in the depths of location of nanocavities, the confined electronic states were in resonance or out of resonance at the chosen bias voltage. The period of oscillation determines the depth of location of the reflective facet calculated by formula 1 using tabulated data on $E(k)$ for copper [46]. The calculated depth is indicated in the upper right corner of each STS spectrum and ranges from 4.5 to 80 nm. Note that the STS spectra and maps in Fig. 6 (a – d) were obtained at 77 K, whereas those presented in Fig. 6 (e – h) were measured at 4.7 K for deeper nano-objects. The calculated depth is consistent with the sum of Ar implantation depth as described in the Experiment section which is within the typical range of 1 nm to 10 nm [47] and the resulting thickness of the copper layer added in increments of 10 nm. The satellite spots in figure 6 are well visible (a – c) at the corresponding depths of 4.5 nm, 12.5 nm and 22.4 nm, respectively, and still recognisable in the pattern (d) at the depth of 32.5 nm. The contour formed by these satellite spots and lines can reveal the size of the buried nanocluster (see similar indication in fig. 5). However, the satellite spots are no longer visible for the deeper nanoclusters, although the main spot is still observable for the depths down to 80 nm (Fig. 6 (e – h)). Their lack of visibility of the satellite spots makes impossible to estimate the size and shape of the buried nanocluster by the way we described above. However, the shape and size of the oblong main spot

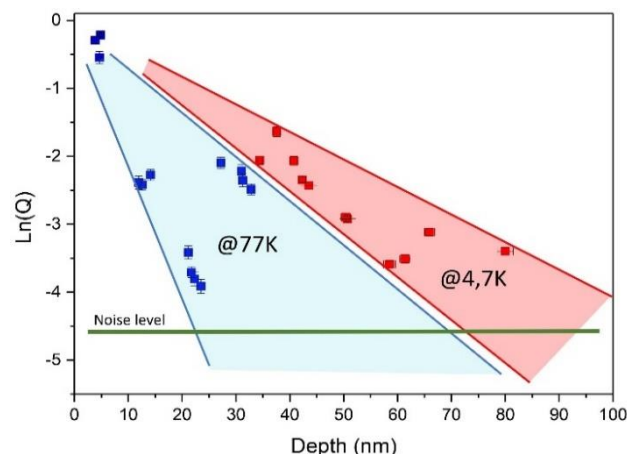


Fig. 7 Amplitude of oscillatory contrast Q of the normalized conductance versus depth d measured at 77 K (in blue) and 4.7 K (in red). Each point corresponds to different nanocluster. Grouping the points with low oscillation amplitude in the range of 10 nm to 25 nm is due to the variation of the tip sensitivity to the oscillatory component of electronic states in some sets of measurements.

corresponding to the electron scattering from the upper (110) facet remains well visible and defined even for depths down to 80 nm (Fig. 6 (h)). Actually, this is sufficient to estimate the size of the hidden nanocluster using an alternative assumption without use of the satellite spots. If we assume the constant ratio between the size of the {110} facets and the size of other facets in the Wulff construction at the different depths, the size of the entire nanocluster can be estimated by only knowing the size of one facet. It is reasonable to assume, as the interface energy is not expected to depend on the location of nanoclusters in the bulk. Usually, near-surface relaxation, which may affect the interface tension, decays within one nanometer [48] while all our Ar nanoclusters lie much deeper. This should support our assumption.

Anyways, we have gotten a direct and impressive confirmation of subsurface STM vision really achieved for the depth of 80 nm (Fig. 6h). Since the signal-to-noise ratio is higher than 1 in both the oscillation plot and the pair of STS images, the STM is able to see even deeper.

In order to determine the ultimate depth of the STM subsurface vision, we have plotted in Fig. 7 the variation of the oscillations amplitude Q of the normalized differential conductance as a function of depth d recorded at the centre of the oblong spot. Indeed, the interpolation of such a plot would give an estimate of such ultimate depth. Data are presented in Fig. 7 for many nanoclusters of identical size to discard size dependency. The measurements were performed at two temperatures: at 77 K for shallow nanoclusters and at 4.7 K for deeper ones. As a consequence, the decay rate must be adjusted for these two temperatures separately. For clarity, data taken at 77 K and 4.7 K are indicated in red and blue, respectively in Fig. 7.

In Fig. 7, if one discard the two sets of data around a depth of 12 and 22 nm as will be discussed below, the intersection between the actual noise level drawn in green in Fig. 7 with the decay rate interpolation would lead to an ultimate depth of roughly 110 nm at 4.7 K and 70 nm at 77 K. The strong attenuation of Q for these two abovementioned sets of data could be explained by different tip termination states that could strongly alter the sensitivity to the oscillatory component of the tunnelling signal. Unfortunately, a particular electronic state at the tip apex is not always controllable and can depend on tip or can be changed over time by intentional or accidental perturbations. Therefore, the ultimate depth deduced from the plot in Fig. 7 may be underestimated and a perfect STM tip with an appropriate electronic state could provide much better results.

The two decay rates at two temperatures indicate that electron-phonon scattering processes influence the coherence of the electronic states. Another temperature effect usually considered when performing STS studies is the thermal broadening of the resonance states. However, in our case, it plays an insignificant role since the periodicity in STS oscillations in our experiments is always much higher than the value of $k_B T/e$ (with k_B , Boltzmann's constant).

We expect similar effect of subsurface vision to occur to other couples of metallic matrix / buried nano-objects. However, performances might depart from the ideal case presented here since it depends strongly on the quality of the interfaces and on the electronic states of both materials. Indeed, the Ar-filled nanoclusters provide total reflection due to the abrupt disappearance of conductance for Ar and exhibit atomically-flat interfaces with copper. The similar configuration could be achieved burying nanoparticles from insulators or semiconductors. Even, if metallic conductive nanoclusters would be used instead of Ar nanoclusters as subsurface nano-objects, the partial electron reflection at interfaces is still possible due to the mismatch of k -vectors of two materials. This should also lead to the oscillating LDOS at the surface and the possibility to observe the metallic subsurface nanoclusters with STM through the surface. The coherent reflection of electrons depends on interface with the nanoparticles as well. The smooth interface across several nanometers can be provided by a choice of growth techniques for a broad class of materials. The ultimate depth of subsurface STM vision with another sort of nano-objects, however, can deviate from the one we reported for the idealized system of Ar nanoclusters in copper, but still can reach the range of a few tens of nanometers according to our partially confirmed expectations. Therefore, we claim our approach to the subsurface STM vision as a promising method for many applications.

Conclusions

We have presented the concept and the experimental proof of deep subsurface vision using STM. Nano-objects hidden below the surface can still be characterised by STM if they are buried up to 110 nm deep. In that sense, it brings bulk sensitivity available to STM which is a method

commonly known to for surface characterization. Our approach is based on the use of near-surface QW states formed in the host material due to the electron confinement between the surface and buried nano-objects. These QW states, probed on the surface by STS, reveal periodic oscillation of LDOS. The spatial variation of oscillatory LDOS carries information about location, size, and shape of buried nano-objects while the oscillation period of LDOS defined by the QW width, determines the depth of hidden nano-object. The effect of electron focusing due to a specific band structure of the host material enhances the ultimate depth of the STM subsurface vision. These results put in evidence that the STM is well suitable for non-destructive 3D characterisation near the surface. Our approach can be applied to other combination of materials.

Author Contributions

O. K. and M. S. contributed equally to this work. O.K. carried out the low-temperature-STM/STS experiments and treated the results. O.K. and M.S. initially wrote the manuscript and all the authors contributed. E.G. performed the theoretical calculations of band structure. O. K. did the sample fabrication at the assistance of D. P.; Y. L. helped at interpretation of QW results. S.M. and O.K. supervised the work. All authors approved the final version of the manuscript.

Conflicts of interest

There are no conflicts to declare.

Acknowledgements

This work was supported by the French PIA project "Lorraine Université d'Excellence" reference ANR-15-IDEX-04-LUE, and by the project CAP-MAT supported by the "FEDER-FSE Lorraine et Massif Vosges 2014–2020", a European Union Program. O.K. was supported by the region Grand Est under the DESOMIN project. O.K. and S.M. acknowledge the financial support of the Institut Carnot ICEEL. We are thankful to Can Avci and Bert Koopmans for their interest at preliminary results, and to Mattijn Cox for offering a graphical illustration for figure 1. We also want to recollect the memory of Karl-Heinz Rieder (1942 – 2017) who appreciated our very first results in private communications and inspired us for going further. Computing resources were provided by the EXPLOR centre hosted by the University de Lorraine.

References

- 1 G. Binnig, H. Rohrer, Ch. Gerber, and E. Weibel, *Phys. Rev. Lett.*, 1982, **49**, 57.
- 2 R. Wiesendanger, *Scanning Probe Microscopy and Spectroscopy: Methods and Applications*, Cambridge, UK: Cambridge University Press, 1994.
- 3 T. Takigami and M. Tanimoto, *Appl. Phys. Lett.*, 1991, **58**, 2288.

- 4 R.S.R. Gajjela, A.L. Hendriks, A. Alzeidan, T.F. Cantalice, A.A. Quivy, and P. M. Koenraad, *Phys. Rev. Mat.*, 2020, **4**, 114601.
- 5 J. Mayer, L.A. Giannuzzi, T. Kamino, and J. Michael, *MRS Bulletin*, 2007, **32**, 400.
- 6 R. Busch, C. Tielemann, S. Reinsch, R. Müller, C. Patzig, M. Krause, and T. Höche, *Micron*, 2021, **150**, 103090.
- 7 Y. Lu, D. Li, and F. Liu, *Materials*, 2022, **15**, 307.
- 8 J. Osing and I.V. Shvets, *Surf. Sci.*, 1998, **417**, 145.
- 9 T. Siahhaan, O. Kurnosikov, H. J. M. Swagten, and B. Koopmans, *Phys. Rev. B*, 2014, **90**, 165419.
- 10 A. Rai, J. Nayak, S.R. Barman, *Appl. Surf. Sci.*, 2015, **332**, 260.
- 11 J. K. Garleff, A. P. Wijnheijmer, and P. M. Koenraad, *Semicond. Sci. Technol.*, 2011, **26**, 064001.
- 12 J.-M. Jancu, J.-Ch. Girard, M.O. Nestoklon, A. Lemaître, F. Glas, Z.Z. Wang, and P. Voisin, *Phys. Rev. Lett.*, 2008, **101**, 196801.
- 13 A.P. Wijnheijmer, J.K. Garleff, K. Teichmann, M. Wenderoth, S. Loth, R.G. Ulbrich, P.A. Maksym, M. Roy, and P.M. Koenraad, *Phys. Rev. Lett.*, 2009, **102**, 166101.
- 14 G. Mahieu, B. Grandidier, D. Deresmes, J.P. Nys, D. Stiévenard, and Ph. Ebert, *Phys. Rev. Lett.*, 2005, **94**, 026407.
- 15 M. Roy and P.A. Maksym, *J. Physics.*, 2014, **526**, 012008.
- 16 I. B. Altfeder, K. A. Matveev, and D. M. Chen, *Phys. Rev. Lett.*, 1997, **78**, 2815.
- 17 J. Kim, S. Qin, W. Yao, Q. Niu, M. Y. Chou, and C.-K. Shih, *Proceed. Nat. Acad. Sci. (PNAS)*, 2010, **107**, 12761.
- 18 J. Kim, S. Qin, Y. Zhang, W. Zhu, and C.-K. Shih, *Surf. Sci.*, 2015, **632**, 174.
- 19 R. Otero, A.L. Vazquez de Parga, and R. Miranda, *Surf. Sci.*, 2000, **447**, 143.
- 20 C. Liu, C. Zhao, S. Zhong, C. Chen, Z. Zhang, Y. Jia, and J. Wang, *Nano Lett.*, 2021, **21**, 9285.
- 21 J.-F. Jia, S.-C. Li, Y.-F. Zhang, and Q.-K. Xue, *J. Phys. Soc. Jap.*, 2007, **76**, 082001.
- 22 M. Müller, N. Néel, S. Crampin, and J. Köger, *Phys. Rev. Lett.*, 2016, **117**, 136803.
- 23 M. Müller, N. Néel, S. Crampin, and J. Köger, *Phys. Rev. B*, 2017, **96**, 205426.
- 24 M.-L. Tao, H.-F. Xiao, K. Sun, Y.-B. Tu, H.-K. Yuan, Z.-H. Xiong, J.-Z. Wang, and Q.-K. Xue, *Phys. Rev. B*, 2017, **96**, 125410.
- 25 A. Weismann, M. Wenderoth, S. Lounis, P. Zahn, N. Quaas, R.G. Ulbrich, P.H. Dederichs, and S. Blügel, *Science*, 2009, **323**, 1190.
- 26 T. Kotzott, M. Bouhassoune, H. Prüser, A. Weismann, S. Lounis, and M. Wenderoth, *New J. Phys.*, 2021, **23**, 113044.
- 27 Ye. S. Avotina, Yu. A. Kolesnichenko, and J. M. van Ruitenbeek, *Low Temperature Phys.*, 2010, **36**, 849.
- 28 S. Lounis, P. Zahn, A. Weismann, M. Wenderoth, R.G. Ulbrich, I. Mertig, P.H. Dederichs, and S. Blügel, *Phys. Rev. B*, 2011, **83**, 035427.
- 29 M. Schmid, W. Hebenstreit, P. Varga, and S. Crampin, *Phys. Rev. Lett.*, 1996, **76**, 2298.
- 30 M. Schmid, S. Crampin, and P. Varga, *J. Electron. Spectrosc. Relat. Phenom.*, 2000, **109**, 71.
- 31 C. Sprokowski and K. Morgenstern, *Phys. Rev. B*, 2010, **82**, 165444.
- 32 M. Ruby, B. W. Heinrich, J. I. Pascual, and K. J. Franke *Phys. Rev. Lett.*, 2015, **114**, 157001.
- 33 O. Kurnosikov, O.A.O. Adam, H.J.M. Swagten, W.J.M. de Jonge, and B. Koopmans, *Phys. Rev. B*, 2008, **77**, 125429.
- 34 O. Kurnosikov, J.H. Nietsch, M. Sicot, H.J.M. Swagten, and B. Koopmans, *Phys. Rev. Lett.*, 2009, **102**, 066101.
- 35 O. Kurnosikov, H.J.M. Swagten, and B. Koopmans, *Phys. Rev. Lett.*, 2011, **106**, 196803.
- 36 O. Kurnosikov, D.V. Kulikov, V.S. Kharlamov, H.J.M. Swagten, and Y.V. Trushin, *Phys. Rev. B*, 2011, **84**, 054109.
- 37 L. Burgi, H. Brune, O. Jeandupeux, and K. Kern *J. Electron. Spectrosc. Relat. Phenom.*, 2000, **109**, 33.
- 38 S. Ogawa, H. Nagano, and H. Petek, *Phys. Rev. B*, 1997, **55**, 10869.
- 39 H.T. Nguyen-Truong, *Appl. Phys. Lett.*, 2016, **108**, 172901.
- 40 U. Mizutani, *Introduction to the electron theory of metals* (Cambridge University Press, New York, 2001), 1st ed.
- 41 P.L. de Andres, F.J. Garcia-Vidal, K. Reuter, F. Flores, *Progr. Surf. Sci.*, 2001, **66**, 3.
- 42 K. Reuter, P.L. de Andres, F. J. Garcia-Vidal, F. Flores, and K. Heinz, *Phys. Rev. B*, 2001, **63**, 205325.
- 43 R. Tran, Z. Xu, B. Radhakrishnan, D. Winston, W. Sun, K.A. Persson, and S.P. Ong, *Sci. Data*, 2016, **3**, 16008.
- 44 K.-T. Chen, W.-Ch. Chang, S.-Ch. Lu, Po-Yu. Yang, and H.-Yu Tuan, *J. Nanomaterials*, 2019, **2019**, 2890162.
- 45 Zh. Ren, N. Liu, B. Chen, J. Li, and D. Mei, *J. Phys. Chem. C* 2018, **122**, 27402.
- 46 G.A. Burdick, *Phys. Rev.*, 1963, **129**, 138.
- 47 J. S. Pan, A. T. S. Wee, C. H. A. Huan, H. S. Tan, and K. L. Tan, *J. Appl. Phys.*, 1996, **79**, 2934.
- 48 P.M. Marcus, X. Qian, and W. Hübner, *J. Phys. Condens. Matter*, 2000, **12**, 5541.